Cancer Nanotechnology

RESEARCH Open Access

Fabrication of manganese-coordinated polyphenol carbon dots for photothermal therapy and immune activation

Yunchao Wu[1†], Jinqian Zhu[2†], Qianzhe Li[2], Mengyu Yang[2], Xin Sun[2], Guojun Zheng[1], Fengyi Du[2] and Miaomiao Zhang[2*]

†Yunchao Wu and Jinqian Zhu have contributed equally to this work

*Correspondence: miaomiao@ujs.edu.cn

[1] Clinical Laboratory, The Third People's Hospital of Changzhou, Changzhou 213001, People's Republic of China
[2] School of Medicine, Jiangsu University, Zhenjiang 212013, People's Republic of China

Abstract

Background: Nanoparticle-based photothermal therapy (PTT) is capable of inducing immunogenic cell death (ICD) and eradicating local tumor via hyperthermia. However, it can hardly prevent tumor recurrence and metastasis owing to inadequate immune activation.

Results: To this end, manganese-coordinated polyphenol carbon dots (MP-CDs) were synthesized by hydrothermal carbonization and metal–polyphenol coordination. This prepared MP-CDs had ultra-small particle size of 5 nm, excellent optical performance, good dispersibility in water and favorable biocompatibility. Under 808 nm near-infrared laser irradiation, the MP-CDs with high photothermal conversion efficiency could kill tumor cells and induce the release of damage-associated molecular patterns (DAMPs) from tumor cells. Notably, the MP-CDs can promote the maturation and antigen presentation ability of dendritic cells (DCs) via manganese-mediated immune activation.

Conclusion: The present work offers a versatile strategy to integrate functional metal into CDs via metal–polyphenol coordination for photothermal/immune therapy.

Keywords: Manganese, Carbon quantum dots, Photothermal therapy, Immunity activation

Introduction

Photothermal therapy (PTT) is a promising and localized tumor treatment that utilizes photosensitizer (PSs) to convert light energy into heat energy under near-infrared (NIR) light irradiation, which caused local hyperthermia allowing highly precise ablation of the tumor (Hya et al. 2021). PTT can kill tumor cells locally and precisely, and reduce non-targeted indiscriminate damage to normal tissue cells in the body. Therefore, PTT is capable of greatly improving the therapeutic effect and reducing the side effects in tumor therapy (Yale et al. 2021). During this process, the necrotic or apoptotic tumor cells release a large amount of tumor-associated antigens (TAAs) and damage-associated molecular patterns (DAMPs) due to the occurrence of immunogenic cell death (ICDs). The therapeutic effectiveness of PTT

mainly depends on the PSs, such as organic compounds, metal sulfides, metal ions, and carbon–nitrogen nanomaterials (Chen et al. 2021; Cuello et al. 2020; Hu et al. 2020; Lu et al. 2021). Among them, carbon dots (CDs) with ultra-small size have attracted great attention due to excellent biocompatibility and tunable physicochemical properties (Faggio et al. 2021; Li et al. 2020a, b, c; Xu et al. 2020; Zhang et al. 2017) (Li et al. 2020a, b, c; Liu et al. 2012; Na et al. 2017). The excellent fluorescence properties of carbon quantum dots endow them with unique advantages in the fields of cell imaging, in situ tracking and tumor targeted therapy (Li et al. 2021; Lu et al. 2019; Ni et al. 2022; Li et al. 2020a, b, c). Yan et al. reported that CDs as effective PSs could absorb the near-infrared light for PTT therapy. Although PTT can destroy local tumor in situ effectively, it fails to inhibit tumor recurrence and metastasis. It has been demonstrated that the release of TAAs and DAMPs induced by PTT failed to elicit an robust anti-tumor immune response, which may be ascribed to the inadequate antigen presentation and low immunity stimulation (Zhao et al. 2021). Therefore, the activation of anti-tumor immune response has become the focus of the current PTT therapy against tumor.

At present, the combination of PTT and immune adjuvants or pathogen-related pattern molecules is considered as an effective strategy against tumor (Bo et al. 2022; Huang et al. 2021; Klinman 2004). DC cells as professional antigen presentation cells (APCs) play a vital role of the prim of T cell-mediated immune response (Liu et al. 2022; Zhang et al. 2021). Recently, a number of cutting-edge studies have found that Mn^{2+} can act as an immune activator to promote DC cells maturation and enhance DC cells antigen presentation ability (Yang et al. 2018a, b). Mengze Lv et al. revealed that Mn^{2+} can enhance the host expression of DNA-sensitive sensor cGAS and its downstream protein STING, so stimulate DC cell maturation and promote the secretion of type I interferon, finally enhance the immune response of tumor-killing cells (Yang et al. 2018a, b). Afterward, Mn^{2+} is reported to promote the activation of cGAS and STING in a comprehensive manner from enhancing cGAMP generation to strengthening cGAMP/STING binding affinity (Hou et al. 2020; Lv et al. 2020; Zhou et al. 2021). In addition, Mn^{2+} can also generate −OH through fenton-like reaction and reduce GSH/GPX4 to induce tumor cell apoptosis (Wang et al. 2018; Xu et al. 2021). Nevertheless, the intrinsic biotoxicity and nonspecific distribution of free Mn^{2+} seriously impaired clinical application due to lack of suitable delivery system.

Our previous study showed that CDs could be served as multifunctional nanoparticles which can integrate therapeutic modalities for tumor treatment (Cai et al. 2021a, b; Cai et al. 2021a, b; Yan et al. 2021). In view of this and above statements, we designed and fabricated a novel Mn^{2+}-coordinated polyphenol CDs (MP-CDs) via hydrothermal carbonization and following metal-phenol coordination. The physical and chemical properties of MP-CDs were characterized. The resultant MP-CDs has the superior photothermal performance to induce the ICD from tumor under 808 nm NIR radiation. More importantly, MP-CDs are capable of promoting the maturation and antigen cross-presentation ability of DCs. This study provides a sample and versatile method to integrate functional metal into CDs for tumor therapy, which further widen the CDs application for biomedical fields.

Materials and methods

Materials

Manganese chloride, glycine, gallic acid were purchased from Aladdin Reagent Co.,Ltd. (Shanghai). Cell counting kit-8 (CCK-8) and 4,6-diamino-2-phenylindole (DAPI) were acquired from Thermo Fisher Scientific. Phosphate buffered saline (PBS), Dulbecco minimum essential medium (DMEM) and fetal bovine serum (FBS) were purchased from Hyclone (Logan, UT, USA). Trypsin was from Sigma-Aldrich (USA). APC anti-mouse CD3, PE anti-mouse CD8a (BioLegend), APC anti-mouse CD11c, FITC anti-mouse CD80 and PE anti-mouse CD86 were obtained from BioLegend (San Diego, USA). HMGB1 (mouse) ELISA kit was purchased form Biovison (USA). ATP assay kit was purchased from Beyotime (China). Unless otherwise specified, all reagents are analytically pure without further purification.

Synthesis of MP-CDs

To prepare the bare CDs, 0.5 g of gallic acid and 0.5 g of glycine was dissolved in 20 mL deionized water. The mixture solution was heated in domestic microwave for 10 min. The black products were resuspended and centrifuged at 2000 g for 10 min to remove the large particles. Then, the suspension was collected for the dialysis (molar weight cut-off 3000) with water change every 12 h. After 3 days of dialysis, the dialysate was free-dried to obtain the bare CDs powder. To prepare the Mn-CDs, the method was the same as the above route unless the addition of manganese chloride at the precursors/Mn^{2+} mass ration of 10:1. To prepare the MP-CDs, the manganese chloride and bare CDs at different mass ratio (1:10, 1:50, 1:100) were dissolved into 20 mL deionized water and adjusted pH to 12 under stirring. Next, the reaction solution was dialyzed for 3 days with water change every 12 h. Finally, MP-CDs power was obtained by free-drying.

Characterizations of MP-CDs

The morphology of the MP-CDs was observed by high-resolution transmission electron microscopy (HRTEM) on a JEM-2100 microscope (JEOL, Tokyo, Japan). The surface chemical component of MP-CDs was analyzed using a Fourier Transform Infrared (FT-IR) Spectrometer (Nicolet Nexus 470; GMI, Franklin, IN, USA). Elemental composition of the MP-CDs was performed by X-ray Photoelectron Spectroscopy (XPS) on Thermo Fisher Nexsa (USA). The optical properties of the MP-CDs were recorded with UV-2450 UV/vis spectrophotometer (Shimadzu, Japan) and Cary Eclipse Fluorometer (Varian, Palo Alto, CA, USA).

Photothermal conversion ability

The photothermal conversion efficiency of the MP-CDs was calculated according to the reported methods (Zhu et al. 2013). Different ratios of MP-CDs (1:10, 1:50, 1:100) were prepared, and the temperature changes within 6 min were recorded under the irradiation of 808 nm NIR laser at power intensity of 1.5 W/cm^2. $MP\text{-}CDs_{1:100}$ solutions with different concentrations (0.25, 0.5, 0.75, 1.0, 1.5, 2.0 mg/mL) were irradiated with 808 nm near-infrared laser at power intensity of 1.5 W/cm^2, and the

temperature changes within 6 min were recorded. MP-CDs$_{1:100}$ with a concentration of 2 mg/mL were irradiated under NIR laser irradiation at different intensities (1.0, 1.5, 2.0 W/cm^2). MP-CDs at 1.5 mg/mL were irradiated by 808 nm NIR laser at power intensity of 2.0 W/cm^2 using the 10-min intermittent on–off method. The calculation formula of photothermal conversion efficiency was as follows:

$$\eta = \frac{hS(\Delta T_{\max,mix} - \Delta T_{\max,H_2O})}{I(1 - 10^{-A808})},$$

$$hS = \frac{\sum_i m_i C_{p,i}}{t} In\theta,$$

$$\theta = \frac{\Delta T}{\Delta T_{\max,mix}}.$$

As shown above, h is the heat transfer coefficient. S is the surface area of the container. $\Delta T_{max,\ mix}$ and $\Delta T_{max,H2O}$ were the temperature change of MP-CDs and H_2O and at the maximum stable temperature. I is the laser power, and A808 is the absorbance value of MP-CDs in aqueous solution at 808 nm wavelength. θ is the dimensionless driving force temperature and is defined as the ratio of ΔT to $\Delta T_{max,\ mix}$.

Biocompatibility of MP-CDs

All animal treatment procedures were carried out in accordance with the administrative rules of the Ministry of health of the people's Republic of China. The blood compatibility was slightly modified according to the literature (Du et al. 2016). After anesthesia, 1 mL of eyeball blood was taken and stored in heparin anticoagulant tube. After centrifugation at 1200 rpm for 15 min, the eyeball blood of mice were washed with PBS for three times to obtain mouse red blood cells (MRBC). Then, MRBC was resuspended in 0.9 mL of PBS and incubated with MP-CDs with concentrations of 5, 10, 25, 50, 100, 200 and 400 μg/mL for 24 h. Water and PBS were used as controls. After centrifugation at 1000 rpm for 5 min, the absorbance of supernatants were measured at 541 nm with UV–visible spectrophotometer. The hemolysis percentage of MP-CDs was calculated by absorbance method.

CCK-8 assay was used to evaluate the cytocompatibility of MP-CDs (Zhang et al. 2019). First, MEF cells or 4T1 cells were seeded into 24-well plates at a concentration of 1.5×10^4/well, and cultured in DMEM medium for 24 h at 37 °C, 5% CO_2. Then, the medium was changed with DMEM medium containing MP-CDs at concentrations of 0, 50, 100, 200, 400, 600, 800 μg/mL. After incubation for 24 h, these cells were washed with PBS three times. 10 μL of CCK-8 and 90 μL of DMEM solution were added to each well for 2 h incubation. The absorbance of each well was detected by UV spectrometer at a wavelength of 450 nm. Nontreated cells (in DMEM) were used as a control, and the relative cell viability (mean ± SD, n = 3) was expressed as (Abs sample − Abs zero sitting)/(Abscontrol − Abszero sitting) × 100%. The experiment was repeated three times independently.

Detection of DAMPs

The localization and distribution of MP-CDs in cells were investigated using confocal cell imaging. The treated 10 mm coverslips were pre-filled into the 24-well plates, and the DC2.4 cells were seeded on the slides. The medium containing 200 μg/mL MP-CDs was incubated with DC2.4 cells for 5 h when the cell mass reaches 60%. After washing with PBS, 0.5 mL of 4% paraformaldehyde was added to each well and fixed at room temperature under 15 min. Each well was washed with PBS, added appropriate amount of DAPI and Lyso tracker working solution for 5 min at room temperature, then washed off the staining solution with PBS. Finally, the coverslips were sealed with neutral resin and the cells were subjected to fluorescence imaging.

4T1 cells co-cultured with MP-CDs (0.8 mg/mL) were seeded in 24-well plates and irradiated under 808 nm laser at power intensity of 1.5 W/cm^2 for 10 min. After being cultured for 12 h, the cell supernatant was collected and centrifuged at 2000 g to remove the cell debris and large particles. The extracellularly released ATP and HMGB1 was measured using ATP Assay Kit and HMGB1 ELISA Kit according to the manufacturer's protocol, respectively.

Flow cytometry analysis

DC2.4 cells were chosen to investigate the effect of MP-CDs on maturation and antigen cross-presentation ability. To characterize the maturation, DC2.4 cells were seeded into 6-well plates at a concentration of 1×10^6 cells/well, and co-cultured with MP-$CDs_{1:100}$ (0, 50, 100, 200, 400 μg/mL) for 24 h. Then, these DC2.4 cells were collected and stained with FITC anti-mouse-CD80 and PE anti-mouse-CD86 for flow cytometry detection. To characterize the antigen cross-presentation ability of DC, DC2.4 cells were pulsed with different concentrations of MP-$CDs_{1:100}$ (0, 50, 100, 200, 400 μg/mL) and an equal amount of ovalbumin for 12 h. After various treatments, DC2.4 cells were collected and stained with PE anti-SIINFEKL-H-2 Kb and FITC anti-mouse-CD11c for flow cytometry detection.

Statistical analysis

Each group of experiments was repeated at least three times independently. All data are presented as mean ± SD. Student T test was used for statistical analysis of the two groups, Statistical comparisons were statistical analyzed by one-way ANOVA. Values of $P < 0.05$ were considered statistically significant.

Results and discussion

Characterization of the MP-CDs

The MP-CDs were successfully prepared by microwave-assisted hydrothermal carbonization and subsequent metal–polyphenol coordination. As shown in Fig. 1A and B, the MP-CDs possessed discrete and quasi-spherical shape with no apparent aggregation. Meanwhile, the MP-CDs had a uniform and ultra-small particle size of 5.1 nm in Fig. 1C. The chemical bonds and functional groups of the MP-CDs were analyzed using Fourier Transform Infrared spectroscopy (FT-IR) in Fig. 1D. Compared with the GA spectrum, the MP-CDs spectrum has a broad characteristic peak of amino

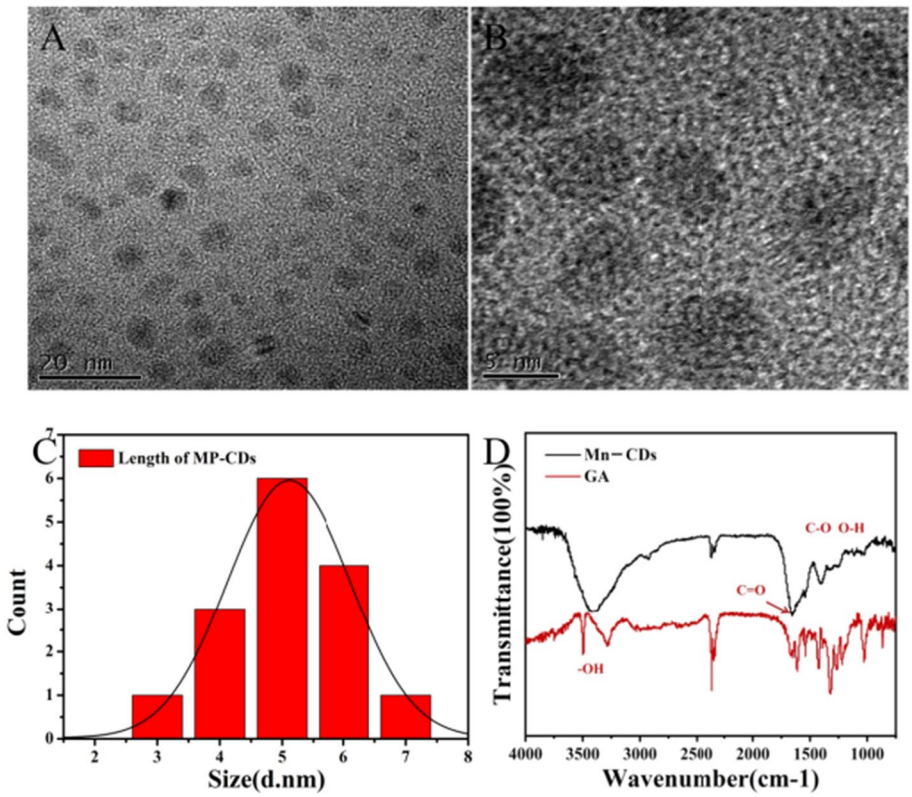

Fig. 1 Characterization of the MP-CDs. **A** TEM image. **B** HRTEM image. **C** Particle size distribution. **D** FT-IR spectrum of MP-CDs

Table 1 Comparison of photothermal conversion efficiency of different MP-CDs with different mass ratios

Mn: CD	Σm	Cp	τs	$\triangle T_{Max,Mix}$	$\triangle T_{Max,Water}$	I(W)	$1-10^{-A\lambda}$	η
1:10	0.2	4.2	135.74	31.8	3.5	1.177	1	14.90%
1:50	0.2	4.2	135.59	32.8	3.5	1.177	1	15.40%
1:100	0.2	4.2	123.03	35.2	3.5	1.177	1	18.40%
bare CDs	0.2	4.2	134.25	38.6	3.5	1.177	1	18.70%

(N–H) or hydroxyl (O–H) stretching vibrations at 3445 cm^{-1}, which was ascribed to GA and glycine as precursors. It was worth noting that the characteristic peak (catechol group) at 3500 cm^{-1} from GA was weak after hydrothermal carbonization. The characteristic peaks at 1630 and 1384 cm^{-1} were attributed to stretching vibration of C = N/C = O and C–O–C, respectively. In brief, the MP-CDs were mainly composed of carboxyl and carbonyl groups, which endowed them with good water dispersibility (Table 1).

Chemical characterization of the MP-CDs

The surface chemical structure of the MP-CDs was analyzed by X-ray Photoelectron Spectroscopy (XPS). As shown in Fig. 2A, there were four distinct main peaks at 300 eV,

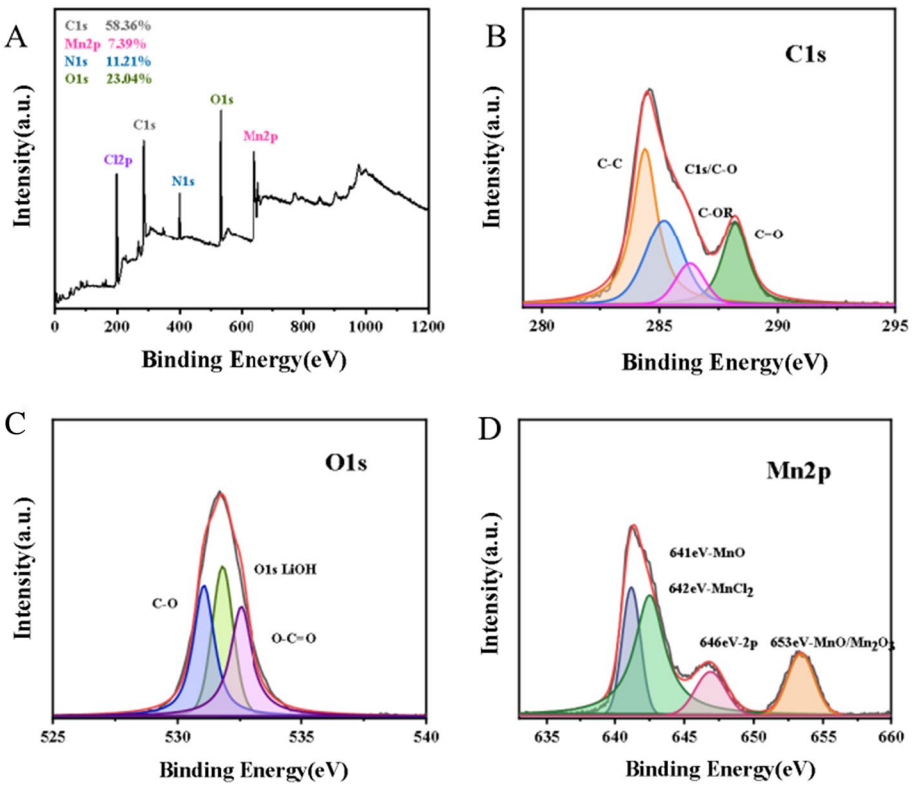

Fig. 2 XPS spectra of the MP-CDs. **A** Survey spectrum, **B** C1s spectrum, **C** O1s spectrum, **D** Mn2p spectrum

400 eV, 520 eV and 650 eV in the total energy spectrum, which were corresponding to C_{1s}, N_{1s}, O_{1s} and Mn_{2p}. It showed that the MP-CDs were mainly composed of C, N, O and Mn elements with the content ratio of 58.4%, 11.2%, 23% and 4.7%. In detail, the binding energy peak of C_{1s} can be deconvoluted into four components at 287, 286, 284 eV, corresponding to C–C, C-O, C-O-R, C = O in Fig. 2B and C. Furthermore, as shown in Fig. 2D, there were four typical binding energy peaks at 641 eV, 642 eV and 653 eV, corresponded to MnO, $MnCl_2$, and Mn_2O_3, which confirmed the presence of Mn element in the MP-CDs. Overall, these findings proved that Manganese ions had been successfully loaded into polyphenol CDs via metal–polyphenol coordination interaction.

Optical characterization of the MP-CDs

The optical properties of MP-CDs were characterized using fluorescence spectroscopy (PL) and ultraviolet spectroscopy (UV/Vis). As shown in Fig. 3A, the MP-CDs exhibited a wide range of emission wavelengths and emission peaks, showed excellent multicolor fluorescence profile. With the gradual increase of the excitation wavelength, the intensity of the emission spectrum first increased and then decreased. Figure 3B showed that the normalized PL spectrum of MP-CDs had a clear red shift. As shown in Fig. 3C, the PL spectrum of the MP-CDs displayed a maximum emission at 476 nm when the maximum excitation wavelength was 396 nm. The MP-CDs solution had a weak absorption peak at 375 nm in the UV–Vis spectrum in Fig. 3D, which might be ascribed to the $\pi \rightarrow \pi^*$ transitions of the conjugated carbon domain. The MP-CDs solution was light brown under

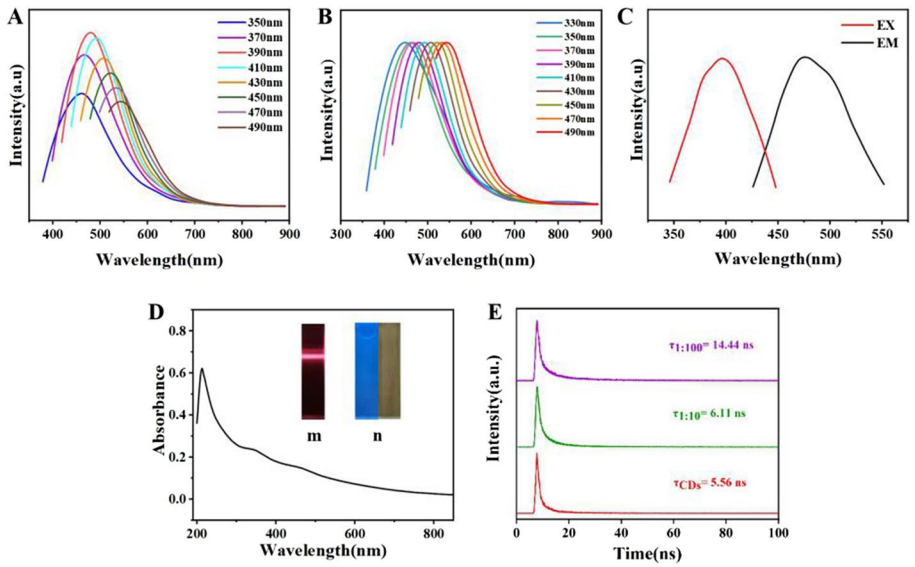

Fig. 3 Optical characterization of the MP-CDs. **A** Fluorescence spectrum and **B** corresponding normalized spectrum. **C** The maximum PL emission and excitation. **D** UV–vis spectrum. Inset: photos of MP-CDs under sunlight and UV irradiation. **E** Time-resolved fluorescence decays of MP-CDs with different doping ratio (Mn:CDs, 1:10, 1:100). The data were collected at an emission peak of 476 nm (λ_{ex} = 373 nm)

sunlight, yet bright blue under ultraviolet light irradiation. Typical Tyndall effect could be observed when a red laser traversed the MP-CDs solution, which fully proved that the MP-CDs aqueous solution was uniform and had good dispersibility in water. Finally, we explored the effect of Mn^{2+} doping on the fluoresce lifetime. In the Fig. 3E, the PL decay curve of bare CDs was well fitted with single exponential decay function, which gave PL lifetime of 5.56 ns. After the addition of Mn^{2+} ions (Mn:CDs, 1:10, 1:100), the lifetime of the CDs was increased to 6.1 and 14.4 ns. The significantly promotion in fluorescence lifetime indicated that strong charge transfer and exciton recombination process occurred, and further confirmed the low electron transfer process in the CDs-Mn^{2+} system (Scheme 1).

Photothermal conversion efficiency of the MP-CDs

To explore the effect Mn^{2+} doping amount on photothermal property, the MP-CDs with distinct Mn/CDs mass ratio of 1:10, 1:50, 1:100 (denoted as MP-$CDs_{1:10}$, MP-$CDs_{1:50}$, MP-$CDs_{1:100}$) as well as Mn^{2+} doped CDs (Mn-CDs) were prepared, respectively. The photothermal properties of these CDs with concentration of 2 mg/mL were characterized under 808 nm laser irradiation at power intensity of 2 W/cm^2 for 6 min. As shown in Fig. 4E, the temperature of aqueous solution kept almost unchanged. Impressively, all of the temperature of CDs solution (CDs, MP-CDs and Mn-CDs) rapidly raised under laser irradiation. The pristine CDs exhibited better photothermal performance than others in which the highest temperature could reach 69.9 ℃. Next, the Mn-CDs was capable of raising the temperature of solution to 64.1 ℃. At last, the temperature of solution containing three kinds of the MP-CDs (1:10, 1:50, 1:100) were 58.6 ℃, 60.5 ℃, 62.6 ℃, indicating the presence of negative correlation between Mn loading and photothermal performance. As shown in Fig. 4A–D, it was an analysis diagram of photothermal

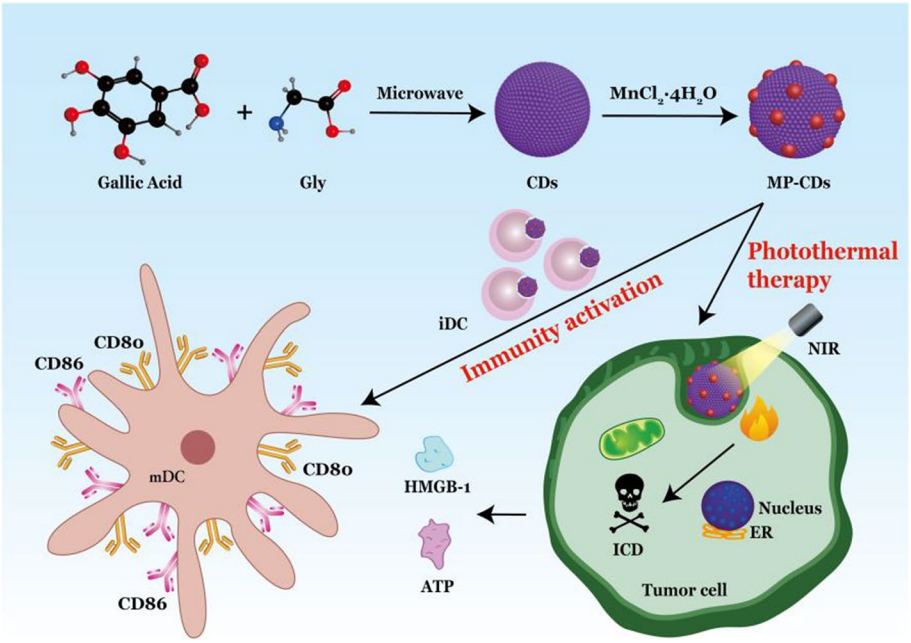

Scheme 1 Schematic illustration of the preparation of MP-CDs and following applications

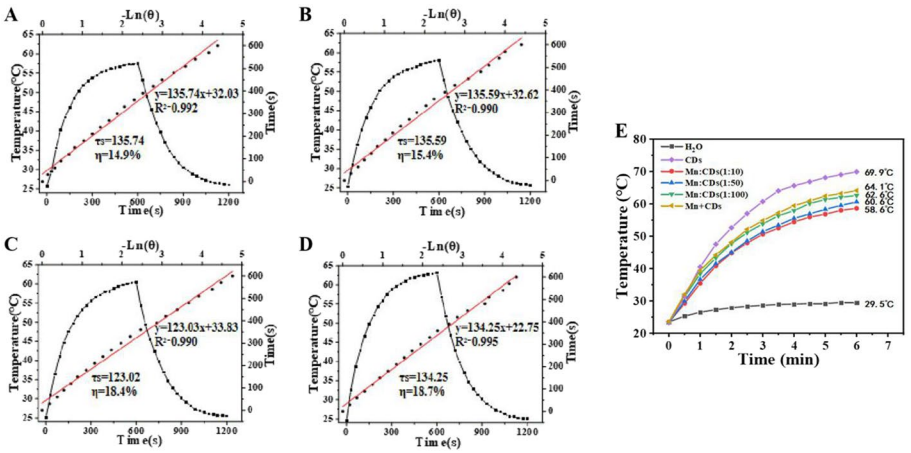

Fig. 4 Calculation of photothermal conversion efficiency of MP-$CDs_{1:10}$ **A** MP-$CDs_{1:50}$ **B**, MP-$CDs_{1:100}$ **C** as well as bare CDs **D** under the 808 nm NIR laser irradiation at power intensity of 2 W/cm^2. **E** Photothermal curves of MP-CDs and Mn-CDs

conversion efficiency of different contents of Mn:CDs. The ratios of Mn to CDs were 1:10, 1:50, and 1:100, respectively. The corresponding τs were 135.74, 135.59, and 123.03, and the thermal efficiencies η were 14.9%, 15.4%, and 18.4%, respectively, which were all less than that in the CDs group (18.7%). To sum up, the doping amount of manganese ions can affect the photothermal conversion efficiency in a negative correlation. The more the amount of manganese ions, the lower the photothermal conversion efficiency. When the ratio was 1:100, the photothermal conversion efficiency was almost the same as that of CDs. In view of this, the MP-CDs (1:100) was chosen for the following applications.

Photothermal conversion performance of the MP-CDs

Subsequently, the effect of power density and concentration on the photothermal performance of the MP-CDs was evaluated. As shown in Fig. 5A, the thermal conversion performance analysis was carried out using different concentrations of MP-CDs solutions under 808 nm NIR at the power density of 1.5 W/cm^2 for 6 min. The temperature of the aqueous solution as a blank control did not change significantly with the extension of the irradiation time. In contrast, the temperature of the MP-CDs solution groups (0.25, 0.50, 0.75, 1.00, 1.50, 2.0 mg/mL) increased with the increasing irradiation time. When the concentration of MP-CDs solution was 2.0 mg/mL, the temperature could rapidly reach 58.5 ℃ in a short time. These findings demonstrated that the higher the concentration of Mn-CDs was, the higher the temperature could rise. As shown in Fig. 5B, the photothermal performance of MP-CDs solution was further explored under different irradiation power densities. When the concentration was 2 mg/mL, the temperature of the MP-CDs solution under the different irradiation power density could rise rapidly. When the power density was 2 W/cm^2, the highest maximum temperature could reach 62.6 ℃. It was a similar trend as concentration, where the higher the power density was, the higher the temperature could rise. However, there was no significant change in the control group. As shown in Fig. 5C, the thermographic image of the recorded MP-CDs further confirmed this phenomenon. As shown in Fig. 5D, the photothermal stability of MP-CDs was further evaluated. The power density was set to 2 W/cm^2, and the irradiation was suspended for 10 min after each 10 min irradiation for repeated 5 times. The research demonstrated that the MP-CDs solution could still be heated to a higher value

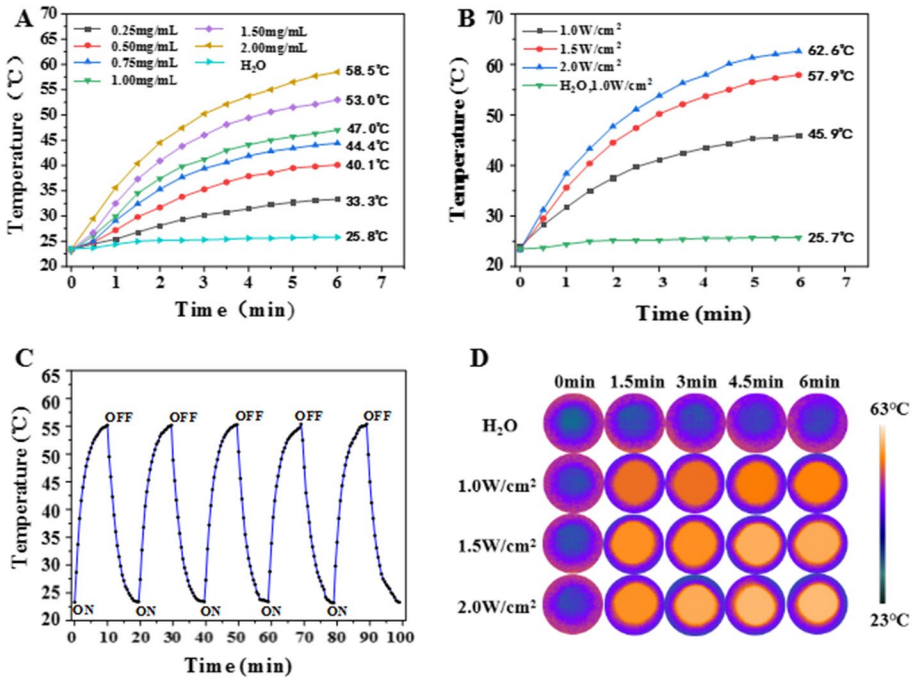

Fig. 5 **A** Temperature curves of MP-CDs solutions with different concentrations and **B** under varied power densities. **C** The corresponding infrared thermal image of MP-CDs solution (800 μg/mL) under 808 nm NIR laser irradiation with varied power densities. **D** Temperature curves of the MP-CDs solutions for five laser on/off cycles under the irradiation of 808 nm NIR laser (2 W/cm^2)

stably and rapidly after multiple NIR irradiation. Meanwhile, the fifth cycle had no obvious thermal efficiency decay compared with the first cycle. These results revealed that MP-CDs had stable photothermal conversion performance.

Biocompatibility of the MP-CDs

The biocompatibility of the MP-CDs was assessed by CCK-8 and hemolytic test. Different concentrations of the MP-CDs were co-incubated with isotonic erythrocytes and then detected using UV spectroscopy. As shown in Fig. 6A, the positive control group (water) showed an obvious absorption peak at 541 nm, which was corresponding to the ultraviolet absorption peak of hemoglobin. The bright red solution indicated that an obvious hemolysis reaction occurred. On the contrary, the negative control group (PBS) and different concentration of the MP-CDs solution group had no obvious absorption peak at 541 nm. When the concentration of the MP-CDs reached the maximum (400 μg/mL), the hemolysis rate was less than 5.0%, which proved that MP-CDs had good blood compatibility and basically did not damage red blood cells. As shown in Fig. 6B, with the increasing concentration of the MP-CDs, there was no obvious hemolysis of red blood cells in the tube, except the control group (water) which had red blood cell hemolysis.

Next, the cytocompatibility of the MP-CDs were evaluated by CCK-8 assay. After co-incubating MEF cells or 4T1 cells with different concentrations (0, 50, 100, 200, 400, 600, 800 μg/mL) of the MP-CDs for 2 h, cell viability was then tested. As shown in Fig. 6C and D, The results shown that both MEF cells and 4T1 cells viability remained stable.

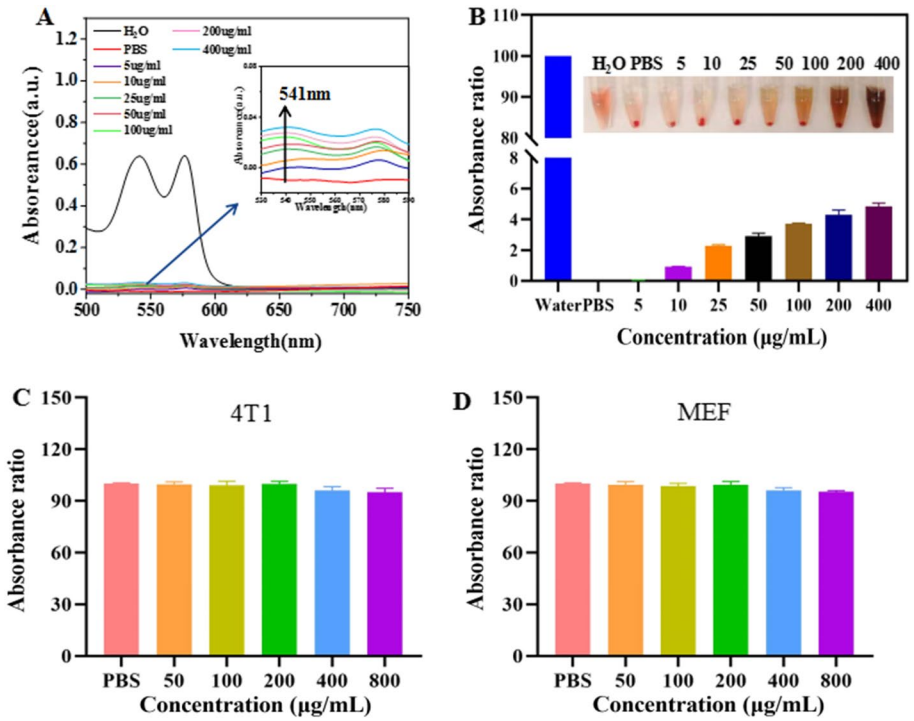

Fig. 6 **A** Hemolytic profile and **B** corresponding statistical chart of red blood cells after incubated with different concentrations of MP-CDs for 2 h. The inset represents photos of red blood cells after treatment. The effect of MP-CDs on the cell viability of MEF cells **C** and 4T1 **D** cells after incubated with different concentrations of MP-CDs for 24 h

Even at the highest concentration of 800 μg/mL, the viability of both cells was greater than 95%. It showed that MP-CDs had favorable cytocompatibility. In addition, the cellular uptake and location of MP-CDs were investigated using laser scanning confocal technique. In Fig. 7A, the green fluorescence could be observed after 4 h and became stronger after 6 h co-incubation with MP-CDs. The co-localization images showed the green fluorescence (MP-CDs) and red fluorescence (Lyso tracker) overlap highly, indicating internalized MP-CDs mainly localized in the lysosome.

MP-CDs induce the ICD to inhibit tumor growth

Increasing evidences had proved that PTT could cause the ICD via hyperthermia, resulting in the damage of tumor cells. As shown in Fig. 7A, the localization of MP-CDs in DC2.4 cells was studied using laser confocal cell imaging. After 5 h of co-culture, the morphology of DC2.4 cells did not change significantly, proved that MP-CDs had good biocompatibility. Moreover, MP-CDs had excellent fluorescence properties and could excite green fluorescence. At the same time, the same location as Lyso tracker in the cell indicated that MP-CDs were mainly distributed in the cytoplasm and cell membrane, and were not seen in the nucleus. As shown in Fig. 7B, the cell viability of 4T1 cells was measured after co-incubation with the MP-CDs under 808 nm NIR irradiation at 2.0 W/cm^2 for 5 min. The results shown that the cell viability of 4T1 cells gradually decreased with the increasing concentration of the MP-CDs. At the concentration of 800 μg/mL, the cell viability was only 17.5%. In order to verify the ICD induced by the MP-CDs, the typical DAMPs (ATP and HMGB1) was measured after PPT. As shown in Fig. 7C and D, the findings demonstrated that the release of both ATP and HMGB1 increased significantly at the concentration of 100 μg/mL. Obviously, MP-CDs was capable of promoting the ATP and HMGB1 release with the increasing concentration. In a short, the MP-CDs

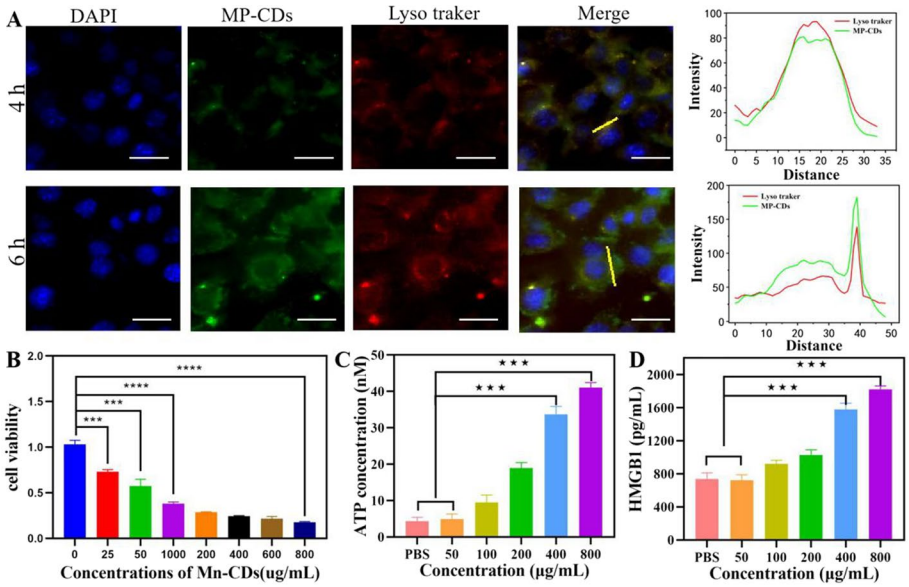

Fig. 7 **A** Fluorescent images of DC2.4 cells incubated with MP-CDs, and corresponding intensity profiles within the regions of interest (green line) of MP-CDs and Lysosome Tracker Red (red line). Scale bars: 20 μm. **B** The effect of MP-CDs on 4T1 cell viability under 808 nm NIR irradiation at 2.0 W/cm^2 for 5 min. **C** The release of extracellular ATP and **D** HMGB1 after PTT treatment

had strong tumor cell-killing ability under NIR irradiation in a concentration-dependent manner, which might be used as ideal PS for photothermal therapy of tumor.

The promotion of MP-CDs on maturation and antigen presentation ability of DCs

Encouraged by Mn^{2+} loading, we proposed that the MP-CDs might have the effect on the maturation and antigen cross-presentation ability of DCs. To this end, the DC2.4 cells were investigated after co-incubation with the MP-CDs using flow cytometry. As shown in Fig. 8, the expression levels of CD80 and CD86 molecules in the untreated DC group were 1.53%. Impressively, the expression levels of CD80 and CD86 molecules on the surface of DC cells gradually increased with the increase of MP-CDs concentrations (0, 50, 100, 200, 400 μg/mL). When the concentration of the MP-CDs was 400 μg/mL, the expression of CD80 and CD86 could reach 11.4%. It was proved that the MP-CDs had a definite effect on promoting DC cells maturation.

The mature DCs could recognize, process and present the tumor antigens to T cells, inducing subsequent anti-tumor immune response. Therefore, the antigen cross-presentation ability of DCs is vital for activation of adaptive immune response. In this study, the SIINFEKL peptides derived from OVA was chosen as molecules model to exploit the antigen cross-presentation ability of DCs. As shown in Fig. 9, the SIINFEKL-H-2 Kb expression was tested after co-incubation with OVA and MP-CDs at different concentration of 0, 50, 100, 200, 400 μg/mL. The results shown that the SIINFEKL-H-2 Kb expression of DC cells increased with the increasing the concentration of the MP-CDs. In the absence of the MP-CDs stimulation, the expression rate of CD86/SIINFEKL-H-2 Kb was only 3.25%. With the increase of concentration of the MP-CDs, the expression rate

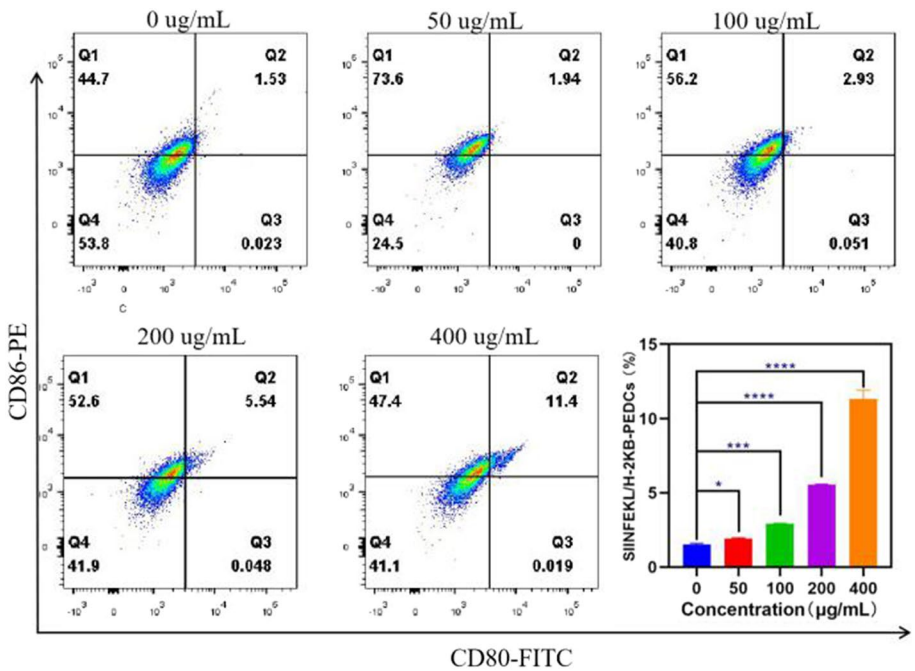

Fig. 8 Flow cytometry for expression levels of $CD80^+$ and $CD86^+$ on the surface of DC2.4 cells incubated with different concentrations of MP-CDs (0, 50, 100, 200, 400 μg/mL) for 24 h and corresponding statistical chart

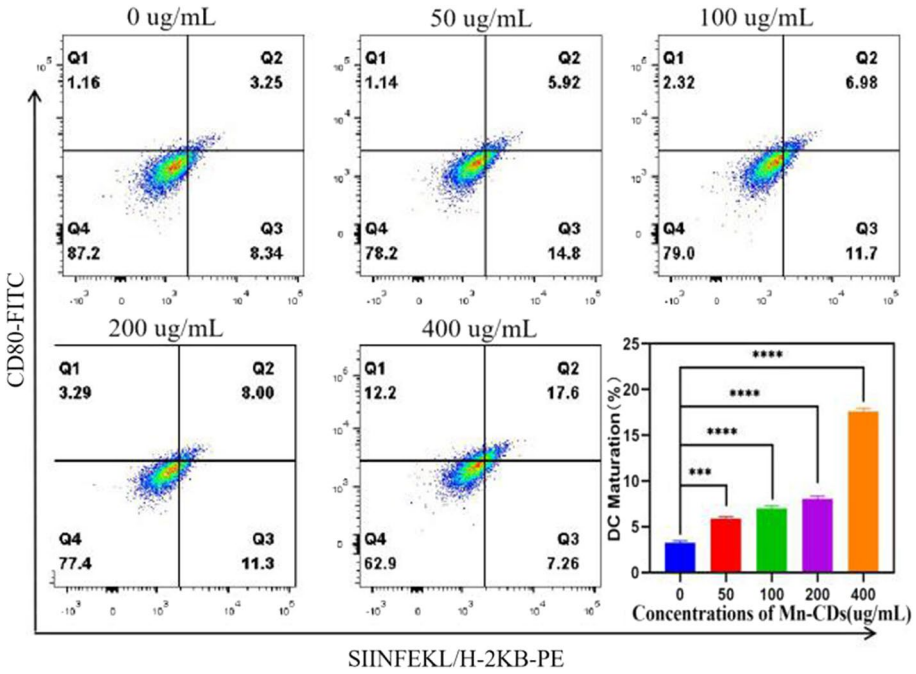

Fig. 9 Flow cytometry of SIINFEKL-H-2 Kb expression on the surface of DC2.4 cells after co-culture with the MP-CDs and OVA, as well as following corresponding statistical chart

increased successively, which were 5.92%, 6.98%, 8.00% and 17.6%, respectively. These findings proved that MP-CDs could effectively stimulate the maturation of DC cells and enhance the antigen cross-presentation ability.

Conclusion

In this study, the MP-CDs were successfully synthesized using gallic acid and glycine as precursors by hydrothermal carbonization and metal–polyphenol coordination. The resultant MP-CDs exhibited simple and high manganese loading, which might be related to the inheritance of polyphenol precursors. Impressively, the MP-CDs possessed superior biocompatibility and photothermal performance. Under NIR irradiation, the MP-CDs could damage tumor cells and induce the release of ATP and HMGB1. Furthermore, the MP-CDs were capable of enhancing the maturation and promoting antigen cross-presentation ability of DCs in vitro. Collectively, this study reported a novel MP-CDs for combined PTT and immune activation against tumor, which widened the functional design of CD in biomedical fields.

Acknowledgements
The Acknowledged are included within the article.

Author contributions
JZ and QL are responsive for experimental operation. YW and MY are responsive for data collection and analysis. XS, GZ are responsive for data processing and drawing. FD and MZ are responsive for experimental design and writing. All authors read and approved the final manuscript.

Funding
The research was supported by Changzhou Sci&Tech Program (Grant No.CJ20200108), Natural Science Foundation of Jiangsu Province (SBK2020022937), Key talents of young medicine in Jiangsu Province (QNRC2016444), Six talent peaks project in Jiangsu Province (No: WSN-281), Zhenjiang key research and development plan (SH2019002), Major natural science research projects of colleges and universities in Jiangsu province (19KJA150004).

Availability of data and materials
The data sets supporting the results of this article are included within the article.

Declarations

Ethics approval and consent to participate
All experimental procedures were approved by the Institutional Animal Care and Use Committee of Medical College of Jiangsu University (NO. UJS-IACUC-AP-20190314002).

Consent for publication
Each coauthor has read the manuscript and approves its submission, and this work is being submitted exclusively to your journal.

Competing interests
The authors declare that they have no known competing financial interests or personal relationships that could have appeared to influence the work reported in this paper.

Received: 21 June 2022 Accepted: 20 September 2022
Published online: 11 October 2022

References

Bo Z, Tc A, Yh A, Zx A, Yj A (2022) Chemo-photothermal immunotherapy for eradication of orthotopic tumors and inhibition of metastasis by intratumoral injection of polydopamine versatile hydrogels. Acta Pharmaceutica Sinica B 12:1447–1459
Cai R, Xiao L, Liu M, Du F, Wang Z (2021a) Recent advances in functional carbon quantum dots for antitumour. Int J Nanomed 13:7195–7229
Cai R, Xiao L, Qiu J, Zhao L, Du F (2021b) Fabrication of cerium doped carbon dots with highly radical scavenging activity alleviates ferroptosis-induced oxidative damage. Nanotechnology. https://doi.org/10.1088/1361-6528/ac0dd9
Chen T, Yao T, Peng H, Whittaker AK, Li Y, Zhu S et al (2021) An injectable hydrogel for simultaneous photothermal therapy and photodynamic therapy with ultrahigh efficiency based on carbon dots and modified cellulose nanocrystals. Adv Funct Mater 31:2106079–2106090
Cuello EA, Abel SB, Barbero C, Yslas I, Molina M (2020) Nanomaterials as photothermal agents for biomedical applications. Sci Rev 1:24–46
Du F, Zhang L, Zhang M (2016) Engineered gadolinium-doped carbon dots for magnetic resonance imaging-guided radiotherapy of tumors. Biomaterials 121:109–120
Faggio G, Grillo R, Foti A, Agnello S, Messina G (2021) Micro-photoluminescence of carbon dots deposited on twisted double-layer graphene grown by chemical vapor deposition. ACS Appl Mater Inter 13:7324–7333
Hou L, Tian C, Yan Y, Zhang L, Zhang Z (2020) Manganese-based nano-activator optimizes cancer immunotherapy via enhancing innate immunity. ACS Nano 14:3927–3940
Hu K, Xie L, Zhang Y, Hanyu M, Zhang MR (2020) Marriage of black phosphorus and Cu2+ as effective photothermal agents for PET-guided combination cancer therapy. Nat Commun 11:2778
Huang T, Li S, Fang J, Li F, Tu S (2021) Antibody-activated trans-endothelial delivery of mesoporous organosilica nanomedicine augments tumor extravasation and anti-cancer immunotherapy. Bioact Mater 6:2158–2172
Hya B, Ming M, Kla B, Jie S, Zl A, Hcab C (2021) A self-assembled metal-polyphenolic nanomedicine for mild photothermal-potentiated chemodynamic therapy of tumors. Appl Mater Today 25:101235–101245
Klinman DM (2004) Klinman, DM. Immunotherapeutic uses of CpG oligodeoxynucleotides. Nat Rev Immunol 4:249–258
Li J, Yang S, Liu Z, Wang G, He P, Wei W et al (2020a) Imaging cellular aerobic glycolysis using carbon dots for early warning of tumorigenesis. Adv Mater 33:2005096–2005102
Li S, Su W, Wu H, Yuan T, Zhou J (2020b) Targeted tumour theranostics in mice via carbon quantum dots structurally mimicking large amino acids. Nat Biomed Eng 4:704–716
Li Z, Wang T, Gu L, Wang H, Zhao Y, Lu S et al (2020c) N-doped carbon dots modified with the epithelial cell adhesion molecule antibody as an imaging agent for HepG2 cells using their ultra-sensitive response to $Al3^{+}$. Nanotechnology 31:485703–485712
Li Z, Ni J, Liu L, Gu L, Wu Z, Li T et al (2021) Imaging-guided chemo-photothermal polydopamine carbon dots for EpCAM-targeted delivery toward liver tumor. ACS Appl Mater Interfaces 13:29340–29348
Liu C, Zhang P, Zhai X, Feng T, Li W, Yang J et al (2012) Nano-carrier for gene delivery and bioimaging based on carbon dots with PEI-passivation enhanced fluorescence. Biomaterials 33:3604–3613
Liu J, Liu S, Wu Y, Xu X, Li Q, Yang M et al (2022) Curcumin doped zeolitic imidazolate framework nanoplatforms as multifunctional nanocarriers for tumor chemo/immunotherapy. Biomater Sci 10:2384–2393
Lu S, Liu L, Wang H, Zhao W, Li Z, Qu Z et al (2019) Synthesis of dual functional gallic-acid-based carbon dots for bioimaging and antitumor therapy. Biomater Sci 7:3258–3265
Lu LA, Xue HA, Mw B, Cl C, Tao JA, Xz A (2021) Recent advances in the development of near-infrared organic photothermal agents. Chem Eng J 417:128844–128862
Lv M, Chen M, Zhang R, Zhang W, Wang C, Zhang Y et al (2020) Manganese is critical for antitumor immune responses via cGAS-STING and improves the efficacy of clinical immunotherapy. Cell Res 30:966–979
Na G, Wen Y, Nie H (2017) Turn-on theranostic fluorescent nanoprobe by electrostatic self-assembly of carbon dots with doxorubicin for targeted cancer cell imaging, in vivo hyaluronidase analysis, and targeted drug delivery. Biosens Bioelectron 96:300–307

Ni J, Kong L, Tang M, Song Y, Zhao J, Wang W et al (2022) Sensitive visual detection of intracellular zinc ions based on signal-on polydopamine carbon dots. Nanotechnology 33:185502–185511
Wang S, Li F, Qiao R, Hu X, Liao H (2018) Arginine-rich manganese silicate nanobubbles as a ferroptosis-inducing agent for tumor-targeted theranostics. ACS Nano 12:12380–12392
Xu A, Wang G, Li Y, Dong H, Yang S, He P et al (2020) Carbon-based quantum dots with solid-state photoluminescent: mechanism, implementation, and application. Small 16:2004621
Xu Q, Zhan G, Zhang Z, Yong T, Gan L (2021) Manganese porphyrin-based metal-organic framework for synergistic sonodynamic therapy and ferroptosis in hypoxic tumors. Theranostics 11:1937–1952
Yale Y, Li F, Li Y (2021) Biomimetic nanoparticles carrying a repolarization agent of tumor-associated macrophages for remodeling of the inflammatory microenvironment following photothermal therapy. ACS Nano 15:15166–15179
Yan H, Zhang B, Zhang Y, Su R, Li P, Su W (2021) Fluorescent carbon dot-curcumin nanocomposites for remarkable antibacterial activity with synergistic photodynamic and photothermal abilities. ACS Appl Bio Mater 4(9):6703–6718
Yang L, Crawford BM, Vo-Dinh T (2018a) Gold nanoparticles-mediated photothermal therapy and immunotherapy. Immunotherapy-UK 10:1175–1188
Yang R, Xu J, Xu L, Sun X, Chen Q, Zhao Y et al (2018b) Cancer cell membrane-coated adjuvant nanoparticles with mannose modification for effective anticancer vaccination. ACS Nano 12:5121–5129
Zhang M, Zhao X, Fang Z et al (2017) Fabrication of HA/PEI-functionalized carbon dots for tumor targeting, intracellular imaging and gene delivery. RSC Adv 7:3369–3375
Zhang M, Zhao L, Du F, Wu Y, Du F (2019) Facile synthesis of cerium-doped carbon quantum dots as a highly efficient antioxidant for free radical scavenging. Nanotechnology 30:325101
Zhang J, Chen C, Li A, Jing W, Sun P, Huang X et al (2021) Immunostimulant hydrogel for the inhibition of malignant glioma relapse post-resection. Nat Nanotechnol 16:538–548
Zhao Y, Baldin AV, Isayev O, Werner J, Zamyatnin AA, Bazhin AV (2021) Cancer vaccines: antigen selection strategy. MDPI AG 9:85–114
Zhou Q, Gong N, Zhang D, Zhu K, Liang P, Liang X (2021) Mannose-derived carbon dots amplify microwave ablation-induced antitumor immune responses by capturing and transferring "danger signals" to dendritic cells. ACS Nano 15:2920–2932
Zhu M, Nie G, Meng H (2013) Physicochemical properties determine nanomaterial cellular uptake, transport, and fate. Acc Chem Res 3:622–631

Publisher's Note